MISSOURI S&T

Missouri University of Science and Technology

Scholars' Mine

Electrical and Computer Engineering Faculty Research & Creative Works

Electrical and Computer Engineering

01 Jan 1998

DC Link Stabilized Field Oriented Control of Electric Propulsion Systems

Keith Corzine
Missouri University of Science and Technology

S. D. Sudhoff

Steven F. Glover

H. J. Hegner

et. al. For a complete list of authors, see https://scholarsmine.mst.edu/ele_comeng_facwork/950

Recommended Citation

DC Link Stabilized Field Oriented Control of Electric Propulsion Systems

S.D. Sudhoff, K.A. Corzine, S.F. Glover
Department of Electrical Engineering
University of Missouri - Rolla

H.J. Hegner, H.N. Robey, Jr.
Naval Surface Warfare Center
Annapolis Detachment, Carderock Division

Abstract - Induction motor based electric propulsion systems can be used in a wide variety of applications including locomotives, hybrid electric vehicles, and ships. Field oriented control of these drives is attractive since it allows the torque to be tightly and nearly instantaneously controlled. However, such systems can be prone to negative impedance instability of the dc link. This paper examines this type of instability and sets forth a readily implemented albeit nonlinear control strategy to mitigate this potential problem.

I. INTRODUCTION

Electric propulsion systems consisting of a turbine driven synchronous machine feeding an induction motor drive through a rectifier - dc link - inverter frequency changer are important in a wide variety of applications including locomotives, hybrid electric vehicles, and ship propulsion systems, including the next generation warship, the Surface Combatant 21. The advantage of such a system over a mechanical transmission is that the turbine speed becomes fully decoupled from the load speed, allowing the turbine speed to be optimized with regard to fuel efficiency. In addition, the elimination of the mechanical linkage between the turbine or other prime mover and the mechanical load (drive train or propeller) allows a greater degree of architectural freedom in the locomotive / vehicle / ship layout. In many of these systems, the inverter is used to tightly regulate the motor current waveforms, which has the advantage of making the inverter / motor drive extremely robust with regard to preventing overcurrents. However, at the same time, such regulation has the disadvantage that it makes the motor drive appear to have a negative impedance [1], since if the inverter voltage is reduced the dc link current will increase so as to maintain constant power (since the motor currents will remain undisturbed). This negative impedance can result in loss of dynamic stability of the propulsion system. In order to avoid instability, one method is to increase the dc link capacitance. However, in large drive systems, such as those used in naval applications, the capacitance required can become costly in terms of space, weight, and maintenance (particularly in regard to identifying shorted capacitors in a large bank). In this paper, a nonlinear dc link stabilized field oriented control is demonstrated which is shown to have performance characteristics similar to the classical field oriented control [2-3], but mitigates the negative impedance instability problem.

II. SYSTEM OVERVIEW

Fig. 1 illustrates the type of electric propulsion system considered herein. The power source of this system is a diesel engine or turbine which serves as a prime mover for the 3-phase synchronous machine (SM). The 3-phase output of the machine is rectified using an uncontrolled rectifier. The rectifier output voltage is denoted v_r. An LC circuit serves as a filter, and the output of this filter is denoted v_{dcs}. A voltage regulator / exciter adjusts the field voltage of the synchronous machine in such a way that the source bus voltage v_{dcs} is equal to the commanded bus voltage v_{dcs}^*. The source bus is connected via a tie line to the load bus, the voltage at which is denoted v_{dci}. The load bus consists of a capacitive filter (which includes both electrolytic and polypropylene capacitance) as well as a 3-phase fully controlled inverter, which in turn supplies an induction motor. The induction motor drives the mechanical load, which is rotating at a speed $\omega_{rm,im}$. Based upon the mechanical rotor speed, and the desired electromagnetic torque $T_{e,des}$ (which is determined by the controller governing the mechanical system), the induction motor controls specify the on/off status of each of the inverter semiconductors in such a way that the desired torque is obtained. Although this system is quite robust with regard to overcurrents, and simple to design from the viewpoint that the controller governing the mechanical system is decoupled from the control of the electrical system (since the torque can be controlled nearly instantaneously), such systems are prone to be subject to a limit cycle behavior in the dc bus voltage known as negative impedance instability [1].

III. CAUSE OF NEGATIVE IMPEDANCE INSTABILITY

In order to gain insight into the cause of negative impedance instability, it is appropriate to set forth a highly simplified model of the system depicted in Fig. 1. This model will focus on the dc link dynamics and need only be valid in the tens to hundreds of hertz frequency band. An appropriate equivalent circuit of the synchronous machine / rectifier and LC filter is illustrated in Fig. 2. Therein, the dynamics of both the prime mover and voltage regulator are neglected since these are subject to long time constants imposed by the prime mover inertia and synchronous machine field, respectively. The dc voltage behind inductance and resistance synchronous machine model is based on the work set forth in [4], which has been shown to have excellent bandwidth. In Fig. 2,

$$E = \omega_{r,sm}\sqrt{\left(\lambda_q''\right)^2 + \left(\lambda_q''\right)^2} \qquad (1)$$

where $\omega_{r,sm}$ is the electrical rotor speed of the synchronous machine and λ_q'' and λ_d'' are the q- and d-axis subtransient flux linkages, α is the firing angle relative to the subtransient back emf, $L_c(\beta)$ and $L_t(\beta)$ are the commutating and transient commutating inductance's defined by

$$L_c(\beta) = \tfrac{1}{2}(L_q'' + L_d'') + (L_d'' - L_q'')\sin(2\beta + \tfrac{\pi}{6}) \qquad (2)$$
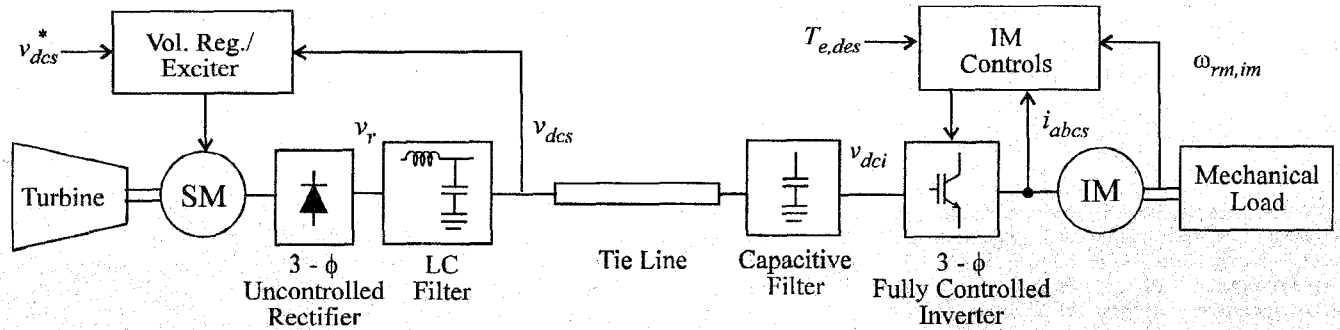
and

Figure 1. Electric propulsion system.

$$L_t(\beta) = L_q'' + L_d'' + (L_d'' - L_q'')\sin(2\beta - \tfrac{\pi}{6}) \qquad (3)$$

where β is the firing angle relative to rotor position and L_q'' and L_d'' are the synchronous machine q- and d-axis subtransient inductances, $r_{s,sm}$ is the synchronous machine stator resistance, L_f and r_f are the inductance and resistance of the LC filter inductor, and C_f is the capacitance of the LC filter capacitor.

A highly simplified model of the capacitive filter and induction motor is illustrated in Fig. 3. Therein, all losses in the machine and inverter are neglected whereupon the drive is modeled as a dependent current source equal to the instantaneous power P divided by dc link voltage v_{dci} and where it is assumed that the instantaneous power is equal to the instantaneous power command P^* defined as

$$P^* = \omega_{rm,im} T_e^* \qquad (4)$$

In (4), T_e^* is an instantaneous torque command which is the input to the field oriented induction motor control. Typically, the instantaneous torque command T_e^* is set equal to the desired torque $T_{e,des}$. However, the control algorithm proposed in this paper will possess an alternate relationship.

Upon neglecting the tie line, which is generally short in an electrical sense for the frequency range of interest, the component models illustrated in Fig. 2. and Fig. 3. are combined as in Fig. 4. Therein,

$$L_e = L_t(\beta) + L_f \qquad (5)$$

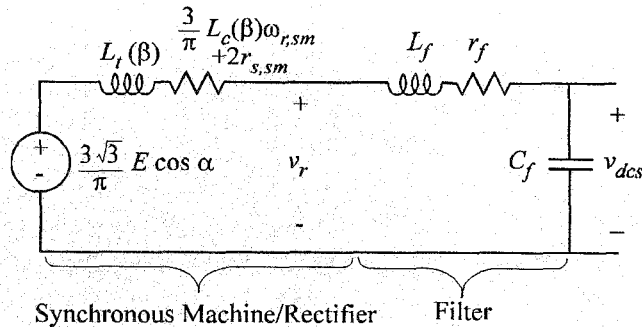$$R_e = \tfrac{3}{\pi} L_c(\beta)\omega_{r,sm} + 2r_{s,sm} + r_f \qquad (6)$$

$$C_e = C_f + C_i \qquad (7)$$

$$v_{es} = \frac{3\sqrt{3}}{\pi} E \cos(\alpha) \qquad (8)$$

In (5-8), α and β can be found by steady-state analysis of the load commutated converter rectifier system as set forth in [5]. However, the calculation can be made much simpler by noting that the rectifier is uncontrolled and by neglecting subtransient saliency whereupon

$$\alpha = 0 \qquad (9)$$

and the commutating and transient commutating inductances are no longer a function of β. Furthermore, due to the action of the voltage regulator, the subtransient inductances will have a value such that

$$v_{es} = v_{es}^* \qquad (10)$$

so that no subtransient information is actually needed. It should be cautioned that this model is intended for explanation purposes and for guidance in designing control algorithms, not for high-fidelity simulation or for the testing of control algorithms.

In order to utilize this equivalent circuit to predict negative impedance stability, note that linearizing the input current with respect to input voltage about an operating point, wherein v_{dci} is equal to v_{dcs}^*, yields

$$\Delta i_{dci} = -\frac{P^*}{v_{dcs}^{*2}} \Delta v_{dci} \qquad (11)$$

from which it is apparent that the small signal inverter input impedance is

$$Z_{inv} = -\frac{v_{dcs}^{*2}}{P^*} \qquad (12)$$

As can be seen, in a small signal sense the inverter appears as a negative resistance which, from an intuitive point of view, would seem to be destabilizing.

Figure 2. Simplified model of synchronous machine/rectifier and filter.
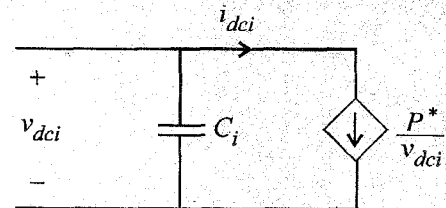

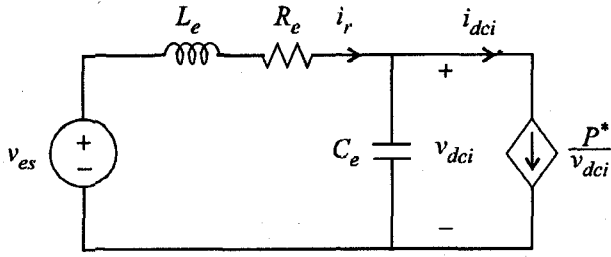Figure 3. Simplified capacitive filter, induction motor drive model.

Figure 4. Highly simplified dc link model.

In order to verify this conclusion, replacing the dependent source representing the inverter with its small signal equivalent impedance yields the following small signal model of the equivalent circuit

$$\frac{d}{dt}\begin{bmatrix} \Delta i_r \\ \Delta v_{dci} \end{bmatrix} = \begin{bmatrix} -\frac{R_e}{L_e} & -\frac{1}{L_e} \\ \frac{1}{C_e} & \frac{P^*}{v_{dcs}^{*2}C_e} \end{bmatrix}\begin{bmatrix} \Delta i_r \\ \Delta v_{dci} \end{bmatrix} + \begin{bmatrix} \frac{1}{L_e} \\ 0 \end{bmatrix}\Delta v_{es}$$

(13)

which has a characteristic equation of

$$\lambda^2 + (\frac{R_e}{L_e} - \frac{P^*}{C_e v_{dcs}^{*2}})\lambda + \left(\frac{1}{L_e C_e} - \frac{P^* R_e}{C_e L_e v_{dcs}^{*2}}\right) = 0 \quad (14)$$

From (14) it follows that necessary conditions for stability are that

$$\frac{v_{dcs}^{*2}}{P^*} > R_e \tag{15}$$

and that

$$\frac{R_e}{L_e} > \frac{P^*}{C_e v_{dcs}^{*2}} \tag{16}$$

Equations (15) and (16) both limit the maximum power command, however (16) is normally the dominant constraint.

In order to avoid negative impedance instability, one method is to simply increase C_e until the system is stable to the maximum possible power command. However, this has the disadvantage in that for very large drive systems the physical size and weight of this capacitance becomes an issue, especially considering the fact that the applications are largely mobile in nature. In addition, large capacitor banks are also undesirable from a maintenance point of view since identifying a shorted capacitor in a large bank is time-intensive. This is significant since electrolytic capacitors have relatively low reliability. In the next section, a control will be set forth which will eliminate the need to increase the capacitance in order to satisfy (16). In addition to ensuring stability, the control can be used to improve damping even if the system is already stable, and, in the case of small drives, may make it possible to entirely eliminate electrolytic capacitance from some systems thereby eliminating one of the traditionally least reliable drive components.

IV. LINK STABILIZING FIELD - ORIENTED CONTROL

In this section, an algorithm which improves the damping of the dc link by eliminating the negative impedance effect over a prescribed bandwidth is set forth. This algorithm is based upon the fact that torque control in a field oriented drive is nearly instantaneous. As mentioned previously, typically the instantaneous torque command T_e^* is set equal to the desired torque $T_{e,des}$ as determined by the control algorithm governing the mechanical

system. However, herein it is proposed to determine the instantaneous torque command as

$$T_e^* = \left(\frac{v_{dci}}{\tilde{v}_{dci}}\right)^n T_{e,des} \tag{17}$$

where v_{dci} is the filtered dc inverter voltage, i.e.,

$$\frac{d\tilde{v}_{dci}}{dt} = \frac{v_{dci} - \tilde{v}_{dci}}{\tau} \tag{18}$$

and the parameters and n and τ are considered to be constants herein but could also be made to be a function of operation point.

The advantage of this readily implemented though nonlinear control algorithm is that it is extremely straightforward to implement yet highly effective in mitigating negative impedance instabilities. In order to illustrate the effect of the algorithm on the system note that using the control law (17) the input power into the inverter is given by

$$P = \left(\frac{v_{dci}}{\tilde{v}_{dci}}\right)^n P_{des} \tag{19}$$

where

$$P_{des} = T_{e,des}\omega_{rm,im} \tag{20}$$

From (19) the input current may be expressed

$$i_{dci} = \frac{v_{dci}^{n-1}}{\tilde{v}_{dci}^n}P_{des} \tag{21}$$

Linearizing (21) about the desired operating point($v_{dci} = \tilde{v}_{dci} = v_{dcs}^*$) yields

$$Z_{inv} = \frac{1}{n-1}\frac{v_{dcs}^{*2}}{P_{des}} \tag{22}$$

If τ is large compared to the time scale of the dc link dynamics and n is selected to be unity then the input impedance presented by the inverter is infinite over the frequency range in which negative impedance instabilities occur, thus avoiding this type of instability.

Although the explanation of the previous paragraph illustrates the basic philosophy of the control, the possibilities of the control are much richer than is indicated therein. In particular, by suitable selection of τ and n a large variety of behaviors can be obtained. In order to see this, it is helpful to first set forth the nonlinear differential equation governing the dc link dynamics in the presence of the new control. In particular,

$$\frac{d}{dt}\begin{bmatrix} i_r \\ v_{dci} \\ \tilde{v}_{dci} \end{bmatrix} = \begin{bmatrix} -\frac{R_e}{L_e} & -\frac{1}{L_e} & 0 \\ \frac{1}{C_e} & 0 & 0 \\ 0 & \frac{1}{\tau} & -\frac{1}{\tau} \end{bmatrix}\begin{bmatrix} i_r \\ v_{dci} \\ \tilde{v}_{dci} \end{bmatrix} + \begin{bmatrix} 0 \\ -\frac{1}{C_e}\frac{P_{des}}{v_{dci}}\left(\frac{v_{dci}}{\tilde{v}_{dci}}\right)^n \\ 0 \end{bmatrix} +$$

$$\frac{1}{L_e}\begin{bmatrix} 1 & 0 & 0 \end{bmatrix}^T v_{es} \tag{23}$$

Linearization of (23) yields

$$\frac{d}{dt}\begin{bmatrix} \Delta i_r \\ \Delta v_{dci} \\ \Delta \tilde{v}_{dci} \end{bmatrix} = \begin{bmatrix} -\frac{R_e}{L_e} & -\frac{1}{L_e} & 0 \\ \frac{1}{C_e} & -\frac{(n-1)}{C_e}\frac{P_{des}}{v_{dcs}^{*2}} & \frac{n}{C_e}\frac{P_{des}}{v_{dcs}^{*2}} \\ 0 & \frac{1}{\tau} & -\frac{1}{\tau} \end{bmatrix}\begin{bmatrix} \Delta i_r \\ \Delta v_{dci} \\ \Delta \tilde{v}_{dci} \end{bmatrix} +$$

$$\frac{1}{L_e}\begin{bmatrix} 1 & 0 & 0 \end{bmatrix}^T \Delta v_{es} \qquad (24)$$

In order to illustrate the effects of varying n and τ, consider the case of a system in which $v_{es}^* = 400$ V, $R_e = 4.58$ Ω, $L_e = 13.9$ mH, and $C_e = 51.4$ μF. These parameters correspond to a test system which was used for laboratory demonstration. Fig. 5 illustrates the root loci of the characteristic equation as τ is varied from 0.1 ms to 1 s for n=1,3,5, and 7 (It should be noted that n does not have to be an integer). As can be seen, in each case the root locus contains an unstable complex pole (denoted A and A*) for small values of τ which becomes stable as τ is increased. For all n shown in Fig. 5 the real part of the eigenvalues becomes more negative as τ in increased. In addition, initially the complex part also decreases. In the case of $n = 5$ eventually the complex pair becomes real (point B) and then one of these real roots meets the root corresponding the filter at point C, at which point this pair of eigenvalues becomes complex. In the case of $n = 7$ the two complex poles eventually become real at point D; after which the pair moves away from each other on the real axis.

Fig. 6 illustrates the damping of the complex pole pair as n and τ are varied. Note that for each value of n there is a value of τ which maximizes the damping. It is also apparent that, generally speaking, as n is increased the damping can be increased.

Since the control law is nonlinear, the eigenvalues will be a function of operating point, and so it is important to investigate the performance of the control as the operating point (primarily through power command) is varied. Fig. 7 illustrates the root locus of the system as power command is varied with $(n = 1, \tau = 4$ ms), $(n = 3, \tau = 2.4$ ms), $(n = 5, \tau = 2.7$ ms), and $(n = 7, \tau = 3.1$ ms). In each case τ was selected so as to maximize the damping factor of the complex pole pair. As can be see from Fig. 7, at low power the complex eigenvalue of the system is at point (A,A*) irregardless of n. In the case of $(n = 1)$, the location of the roots is power level independent. However, in the case of $n = 3$ the complex pair moves to (B,B*). Finally, in the case of $n = 5$, and $n = 7$, the complex eigenvalues become real at point C and D, respectively. This illustrates an important feature of the proposed control law which is that although with the standard control $(n = 0)$ the system becomes less stable as the power level increases, with the proposed control law the system actually becomes more stable as the power level increases, with the
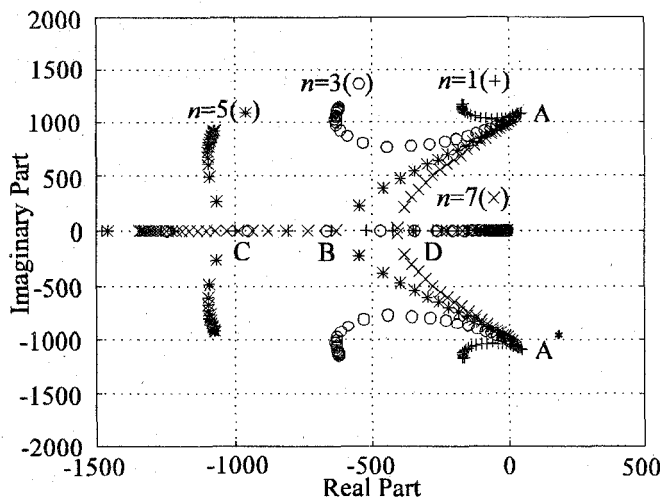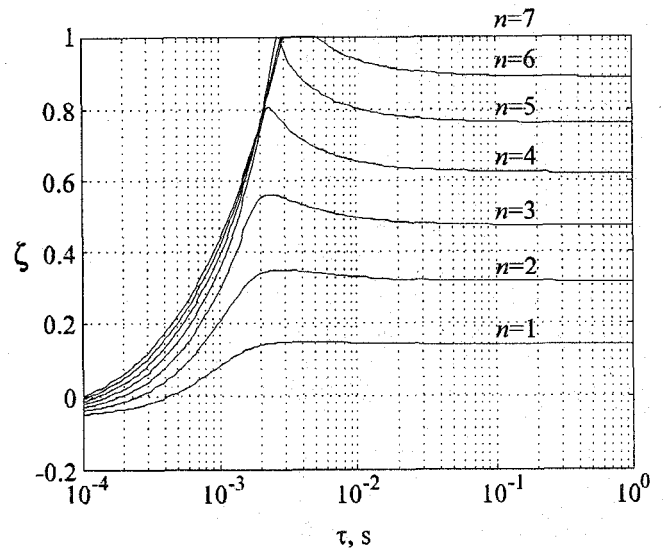

Figure 6. Damping factor versus τ and n.

exception of $(n = 1)$ in which case the eigenvalues associated with the dc link become largely operating point invariant.

V. IMPLEMENTATION

Before setting forth the implementation of the proposed controller, it is appropriate to first consider a standard field oriented control such as the rotor flux indirect field oriented control illustrated in Fig. 8 (note that the control proposed in this paper, is, however, independent of whether or not the field oriented control is direct or indirect). Therein, an instantaneous torque command T_e^* is the input to the controller. This torque command is equal to the torque desired by the controller governing the mechanical dynamics, $T_{e,des}$. As can be seen, based on the torque command T_e^* and desired d-axis rotor flux level λ_{dr}^{e*}, the desired q- and d- axis stator currents, i_{qs}^{e*} and i_{ds}^{e*}, are determined. This calculation is a function of the induction motor magnetizing inductance L_m, the induction motor rotor inductance (rotor leakage plus magnetizing) L_{rr}', the rotor resistance

Figure 5. Root Locus as τ and n are varied.

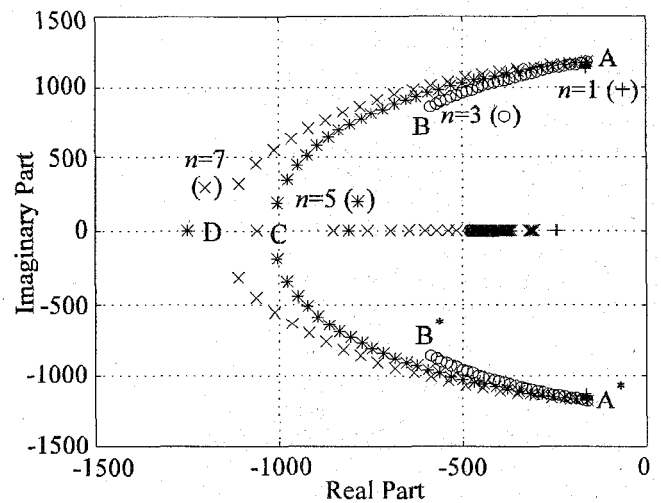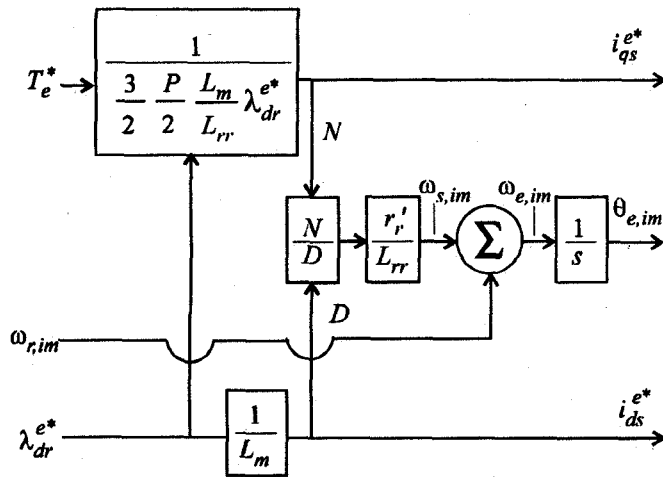

Figure 7. Root locus versus P^* and n.

Figure 8. Rotor flux oriented indirect field oriented control.

r_r', and the number of poles, $N_{p,im}$. Based on the q- and d- axis stator currents the electrical radian slip frequency, $\omega_{s,im}$, is determined, which is then added to the electrical rotor speed $\omega_{r,im}$ in order to determine the electrical speed of the synchronous reference frame $\omega_{e,im}$, which is integrated in order to determine the position of the synchronous reference frame $\theta_{e,im}$. In addition to the algorithm illustrated in Fig. 8, especially in large drives, the field oriented control will often include on line parameter identification algorithm to compensate for variations of the rotor time constant [6-7].

Once the q- and d-axis current commands and the position of the synchronous reference frame are established, these currents may be synthesized in a variety of ways. Herein, the q- and d-axis current command was transformed back into a abc variable current command which is an input to a hysteresis type current control.

Incorporating the link stabilizing control into the field oriented control is quite straightforward. In particular, the only difference in the control is that the instantaneous torque command is generated using (16) rather than being set equal to the desired torque, as is illustrated in Fig. 9.

VI. EXPERIMENTAL SETUP

In order to illustrate the experimental set up a system such as the one depicted in Fig. 1 was constructed at a low (3.7 kW) power level. The prime mover was a dynamometer in speed control mode. The parameters of the 3.7 kW synchronous machine are listed in Table 1. Therein, all rotor parameters have been referred to the
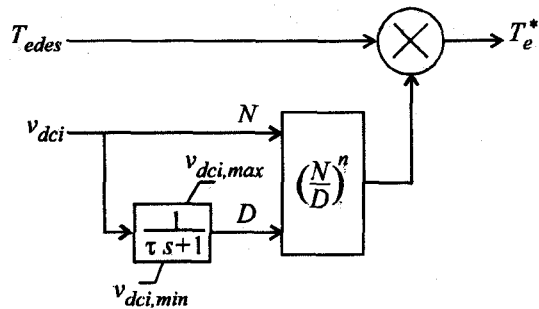
stator by the appropriate turns ratio. A solid state voltage regulator/exciter was used to control the dc link voltage; a block diagram of this control appears in Fig. 10. The LC filter, transmission line, and inverter capacitance parameters are listed in Table 2. The reader will note that the capacitor values are small for this power rating; this was necessary to mimic conditions which exist on much larger drives used for ship propulsion. Finally, a 3.7 kW induction motor was used as a load. Induction motor parameters are listed in Table 3. The induction motor control was implemented based on the indirect rotor flux strategy with a rotor flux linkage command of 0.45 Vs, and the current command was synthesized using hysteresis current control with a hysteresis band of 0.95 A. The link stabilizing controller parameters were $n = 1$, $\tau = 4$ ms, $v_{dcmin} = 200$ V, and $v_{dcmax} = 600$ V.

VII. VALIDATION

The performance of the link stabilizing field oriented control was validated using both a detailed (as opposed to average value / reduced order) computer simulation and in hardware tests. For the purposes of computer simulation, the synchronous machine and induction motor models used were those set forth in [8]. In the case of the salient pole synchronous machine, magnetic saturation was represented in the d-axis. The simulation included the switching of each power semiconductor device. Semiconductor conduction losses were included though switching losses were neglected.

Table 1. Synchronous machine parameters		
$r_{s,sm} = 382$ mΩ	$L_{ls} = 0.83$ mH	$P = 4$
$L_{mq} = 13.5$ mH	$L_{md} = 39.7$ mH	$n_{sfd} = 0.0271$
$r_{kq1} = 31.8$ Ω	$L_{lkq1} = 6.13$ mH	$r_{fd} = 122$ mΩ
$r_{kq2} = 0.923$ Ω	$L_{lkq2} = 3.4$ mH	$L_{lfd} = 2.54$ mH
$r_{kd1} = 40.47$ Ω	$L_{lkd1} = 4.73$ mH	
$r_{kd2} = 1.31$ Ω	$L_{lkd2} = 3.68$ mH	

Table 2. Passive component parameters.		
$L_f = 9.17$ mH	$r_f = 3.01$ Ω	$C_f = 10.1$ μF
$L_{line} = 28.8$ μH	$r_{line} = 273$ mΩ	$C_i = 41.3$ μF

Table 3. Induction motor parameters.		
$r_s = 400$ mΩ	$L_{ls} = 5.73$ mH	$L_m = 64.3$ mH
$r_r' = 227$ mΩ	$L_{lr}' = 4.94$ mH	$N_p = 4$

Figure 9. DC link stabilizing control.
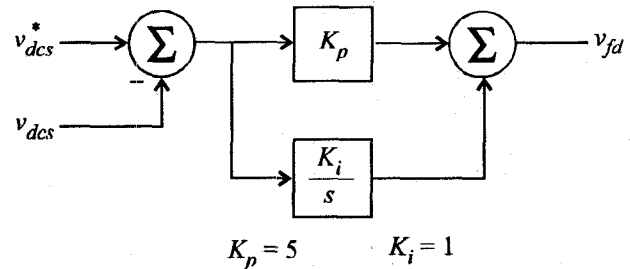

$K_p = 5$ $K_i = 1$

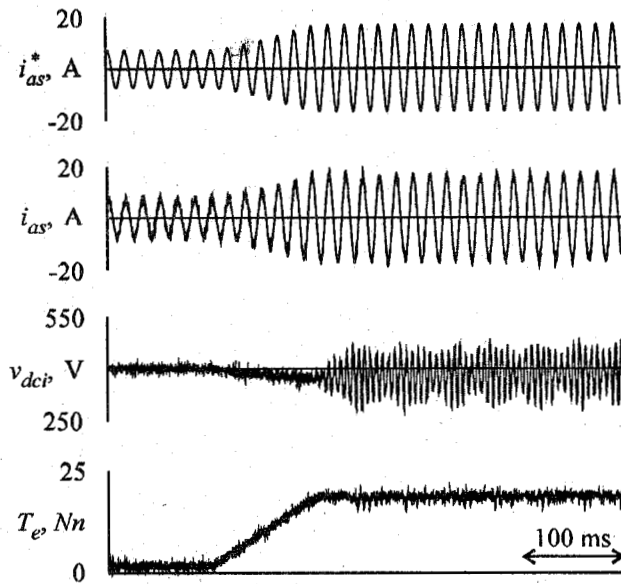Figure 10. Voltage regulator/exciter.

Figure 11. Simulated performance of standard field oriented control during ramp increase in desired torque.
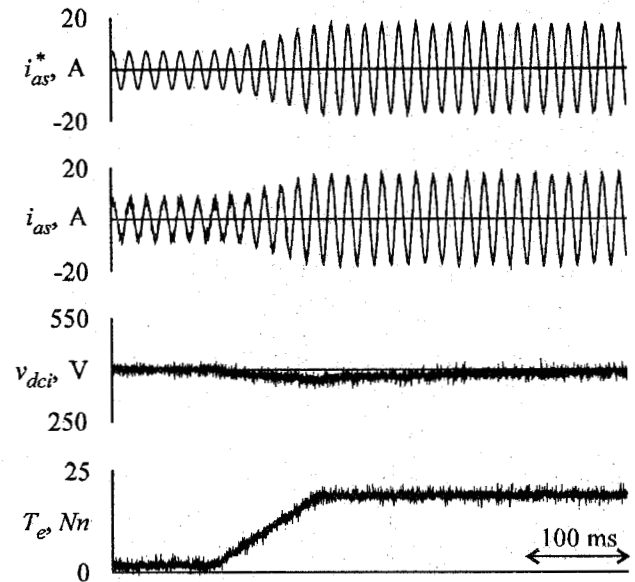

Figure 13. Simulated performance of link stabilized field oriented control during ramp increase in desired torque.
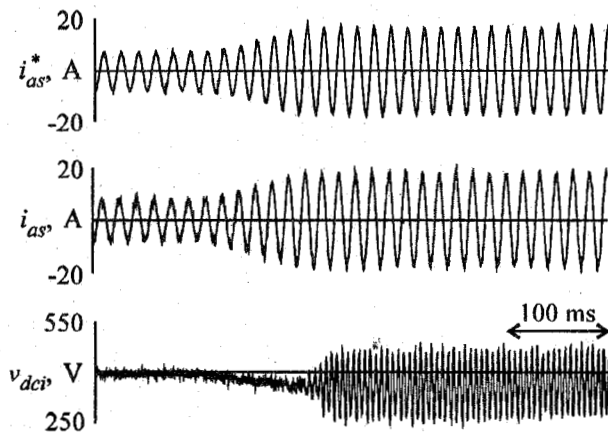

Figure 12. Measured performance of standard field oriented control during ramp increase in desired torque.
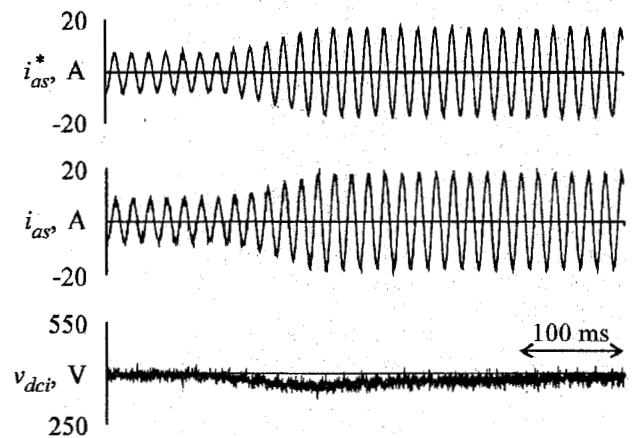

Figure 14. Measured performance of link stabilized field oriented control during ramp increase in desired torque.

Figure 11 illustrates the simulated performance of the system as the desired torque is changed from 2 to 19 Nm over a period of 100 ms. Variables depicted include the commanded a-phase current i_{as}^*, the actual a-phase current i_{as}, the dc inverter voltage v_{dci}, and the electromagnetic torque T_e. Although the actual torque closely tracks the desired torque, it can be seen that as the torque and hence power command increases the dc bus voltage becomes unstable, stressing both the semi-conductors and the capacitors. In a typical system, such behavior could easily result in the semiconductor and/or capacitor failure. The experimental system has been constructed so as to be able to survive the overvoltages. Fig. 12 depicts the same study as measured in the laboratory. In Fig. 12, the instantaneous electromagnetic torque is not shown because suitable instrumentation was not available. As can be seen there is a reasonable correspondence between Fig. 11 and Fig. 12 with the exception that

the actual system appears to be less stable than is predicted by the simulation. This is because the power requirements of the actual drive system are greater than the simulated system because of switching losses (It should be noted that the magnitude of the voltage swing increases very rapidly with power level). In addition, once a system becomes unstable it tends to be very sensitive to parameter variations.

Fig. 13 depicts the performance of the same system with the link stabilizing field oriented control as calculated using the computer simulation. As can be seen, according to the simulation the torque still closely tracks the commanded torque. Furthermore, in this case there is no evidence of instability. Fig. 14 illustrates the system performance as measured in the laboratory. As predicted, the dc bus voltage is well behaved and the dc link bus voltage is stable.
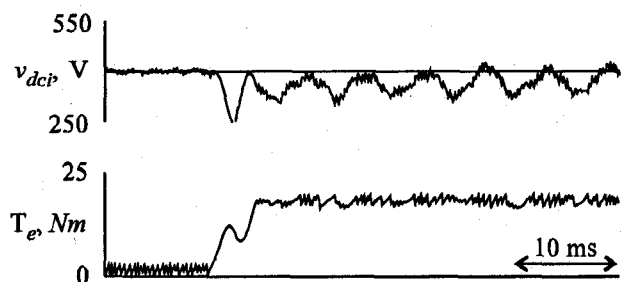
Figure 15. Simulated performance of standard field
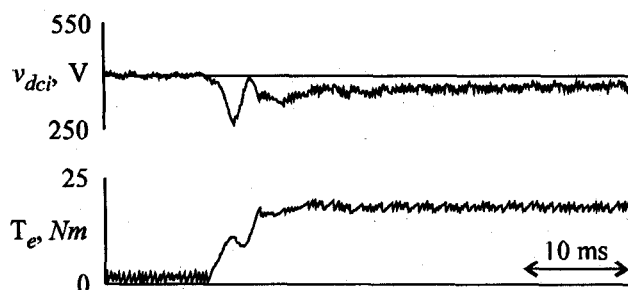oriented control during step change in
desired torque.

Figure 16. Simulated performance of link stabilized
field oriented control during step change
in desired torque.

One concern which may arise is a possible reduction in torque bandwidth since a drop in inverter voltage will result in a transient dip in torque. The detailed computer simulation was used to investigate this effect since the primary variable of interest was the electromagnetic torque. Fig. 15 depicts the predicted change of performance of the standard field oriented control as the torque command is stepped from 2 to 19 Nm. As can be seen, the electromagnetic torque reaches the commanded value in approximately 5 ms. The torque response is not instantaneous due to the fact that a step change in current cannot be achieved in practice and because the dip in link voltage causes a temporary loss of current tracking in the hysteresis current control. Fig. 16 depicts the response of the link stabilized field oriented control. In this case, the electromagnetic torque reaches the commanded value in the order of 8 ms. Although the link stabilized control is somewhat slower than the standard field oriented control, this slight reduction in bandwidth is not a significant disadvantage in view of the improved dc bus voltage. This is particularly true in the fact that most propulsion systems have mechanical inertia such that in either case the torque response may be considered to be instantaneous.

VIII. CONCLUSIONS

A straightforward but nonlinear control algorithm has been set forth which can be used to mitigate negative impedance instabilities in electric propulsion systems. The effectiveness of the control has been demonstrated both through the use of computer simulation and in the laboratory. In addition to being applicable to induction motor

based drives, the control algorithm could also be used with other types of machines in which rapid torque control is possible, most notably permanent magnet synchronous machines.

X. REFERENCES

[1] R.D. Middlebrook, "Input Filter Considerations in Design and Application of Switching Regulators," IEEE Proc. IASAM, 1976.

[2] F. Blashke, "The principle of field-orientation as applied to the new 'transvektor' closed-loop control system for rotating-field machines," Siemens Review, Vol. 34, No. 5, 1972, pp. 217-220.

[3] D.W. Novotny, and R.D. Lorenz, "Introduction to Field Orientation and High Performance AC Drives," Tutorial Course, IEEE Industrial Applications Society, 2nd Ed. 1986.

[4] S.D. Sudhoff, K.A. Corzine, H.J. Hegner, D.E. Delisle, "Transient and Dynamic Average-Value Modeling of Synchronous Machine Fed Load-Commutated Converters," accepted for IEEE Trans. on EC.

[5] S.D. Sudhoff, O. Wasynczuk, "Analysis and Average-Value Modeling of Line-Commutated Converter - Synchronous Machine Systems," IEEE Trans. on EC., Vol. 8, No. 1, March 1993, pp. 92-99.

[6] D.J. Atkinson, P.P. Acarnley, and J.W. Finch, "Observers for induction motor state and parameter estimation," IEEE Trans. on Industry Applications, Vol. 27, No. 6, 1991, pp. 1119-1127.

[7] J. Holtz, T. Thimm, "Identification of machine parameters in a vector-controlled induction motor drive," IEEE Trans. on Industry Applications, Vol. 27, No. 6, 1991, pp. 1111-1118.

[8] P.C. Krause, Analysis of Electric Machinery, McGraw Hill, 1986.

Scott D. Sudhoff received the BSEE, MSEE, and Ph.D. degrees at Purdue University in 1988,1989, and 1991, respectively. He is currently an Assistant Professor at the University of Missouri - Rolla. His interests include electric machines, electric drive systems, power electronics, flexible ac transmission, and finite-inertia power systems. He has authored or co-authored over 20 papers in these areas.

Keith A. Corzine received the BSEE and MSEE degrees from the University of Missouri-Rolla in 1992 and 1994, respectively, and is currently pursuing the Ph.D. degree. His interests include the design and analysis of electric machinery and electric drive systems. He has authored or co-authored 5 transactions papers in these areas.

Steven F. Glover received the BSEE and MSEE degrees from the University of Missouri in 1995 and 1996, respectively. His interests include electric drive systems, power electronics, and automatic control.

Henry J. Hegner received the BSEE degree from Virginia Polytechnical Institute and State University in 1983 and MSEE from Purdue University in 1992. Mr. Hegner is employed within the Electrical Systems Department of the Machinery Research and Development Directorate at the Naval Surface Warfare Center in Annapolis, Maryland. For the past 16 years, Mr. Hegner has specialized in electrical systems and components for shipboard systems. He is currently a member of the U.S. Navy's Advanced Surface Machinery Programs, where he is serving as Teal Leader for the DC Zonal Electrical Distribution System and is a member of the Integrated Power System development teams.

Henry N. Robey, Jr. received the BSEE and MSEE degress from John Hopkins University in 1972 and 1978, respectively. He currently employed as Chief Scientist for Advanced Surface Machinery Programs at the Naval Surface Warfare Center in Annapolis, Maryland. His interests include system engineering, control, and systems simulation.